UC Berkeley
UC Berkeley Previously Published Works

Title

Attosecond Probing of Coherent Vibrational Dynamics in CBr4.

Permalink

https://escholarship.org/uc/item/8v11p4ss

Journal

The Journal of Physical Chemistry A, 128(42)

Authors

Ou, Jen-Hao

Hait, Diptarka

Rupprecht, Patrick

et al.

Publication Date

2024-10-24

DOI

10.1021/acs.jpca.4c05210

Peer reviewed

Article

Attosecond Probing of Coherent Vibrational Dynamics in CBr$_4$

Published as part of The Journal of Physical Chemistry A special issue "Richard J. Saykally Festschrift".

Jen-Hao Ou, Diptarka Hait, Patrick Rupprecht, John E. Beetar, Todd J. Martínez, and Stephen R. Leone*

Read Online

ACCESS | Metrics & More | Article Recommendations | Supporting Information

ABSTRACT: A coherent vibrational wavepacket is launched and manipulated in the symmetric stretch (a$_1$) mode of CBr$_4$, by impulsive stimulated Raman scattering (ISRS) from nonresonant 400 nm laser pump pulses with various peak intensities on the order of tens of 10^{12} W/cm^2. Extreme ultraviolet (XUV) attosecond transient absorption spectroscopy (ATAS) records the wavepacket dynamics as temporal oscillations in XUV absorption energy at the bromine M$_{4,5}$ 3d$_{3/2,5/2}$ edges around 70 eV. The results are augmented by nuclear time-dependent Schrödinger equation simulations. Slopes of the (Br 3d$_{3/2,5/2}$)$^{-1}$10a$_1$* core-excited state potential energy surface (PES) along the a$_1$ mode are calculated to be −9.4 eV/Å from restricted open-shell Kohn−Sham calculations. Using analytical relations derived for the small-displacement limit and the calculated slopes of the core-excited state PES, a deeper insight into the vibrational dynamics is obtained by retrieving the experimental excursion amplitude of the vibrational wavepacket and the amount of population transferred to the vibrational first-excited state as a function of pump-pulse peak intensity. Experimentally, the results show that XUV ATAS is capable of resolving oscillations in the XUV absorption energy on the order of a few to tens of meV with tens of femtosecond time precision. This corresponds to change in C−Br bond length on the order of 10^{-4} to 10^{-3} Å. The results and the analytic relationships offer a clear physical picture, on multiple levels of understanding, of how the pump-pulse peak intensity controls the vibrational dynamics launched by nonresonant ISRS in the small-displacement limit.
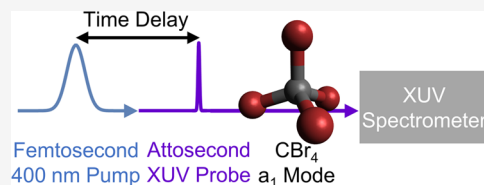
1. INTRODUCTION

Preparing and controlling vibrational coherent superposition states (referred to as vibrational wavepackets) in molecules with light is a major theme in light−matter interactions.[1,2] This necessitates control over the creation, detection, and manipulation of the vibrational wavepacket.[1,2] In this work (Figure 1), such control is achieved in the carbon tetrabromide (CBr$_4$) molecule by attosecond transient absorption spectroscopy (ATAS).[3−5] We employ a 400 nm 26 fs pump laser pulse to generate a vibrational wavepacket in the symmetric stretch (a$_1$) mode of the electronic ground state of CBr$_4$ with nonresonant impulsive stimulated Raman scattering (ISRS).[6−8] The resulting vibrational wavepacket dynamics are subsequently monitored by time-resolved absorption of attosecond extreme ultraviolet (XUV) probe laser pulses at the Br M$_{4,5}$ 3d$_{3/2,5/2}$ edge around 70 eV, recorded as temporal oscillations in the XUV absorption energy. Alternatively, in the electronic state picture, the XUV probe corresponds to the absorption from the electronic ground state to the (Br 3d$_{3/2,5/2}$)$^{-1}$10a$_1$* electronic core-excited states. Here the −1 superscript notation indicates the excitation from that core orbital to the 10a$_1$* orbital.

Similar vibrational dynamics in various molecules have been experimentally observed via electronic core-level transient absorption spectroscopy probed at XUV or soft X-ray regions.[5,9−28] Vibrational wavepackets were triggered by pump pulses mostly in the infrared (780, 800, 1200, or 1600

nm)[9−21,25−28] while some are in visible[22] or UV[23,24] spectral regions. Among them, pump pulses with high ($\sim10^{14}$ W/cm^2) peak intensity[9,10,12−20,27,28] often lead to large vibrational amplitudes. In particular, relatively few works[26,27] systematically measured how the pump-pulse peak intensity affects vibrational dynamics. In this work, 400 nm pulses with lower peak intensities ($8.1-20.2 \times 10^{12}$ W/cm^2) are employed, and the dependence of vibrational dynamics on pump-pulse peak intensity is investigated in the small-displacement limit.[26]

To gain a deeper understanding, it is valuable to explicitly demonstrate how the temporal oscillations in the XUV absorption energy connect the shape of the corresponding core-excited state potential energy surface (PES) with aspects of the vibrational wavepackets, such as the excursion amplitude of the wavepacket and populations in the vibrational eigenstates. To clearly establish these connections, we derive analytical relations for the above quantities in the small-displacement limit with the harmonic approximation. We compute the slope of the Br 3d core-excited state PES along the symmetric stretch mode at the ground state equilibrium
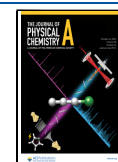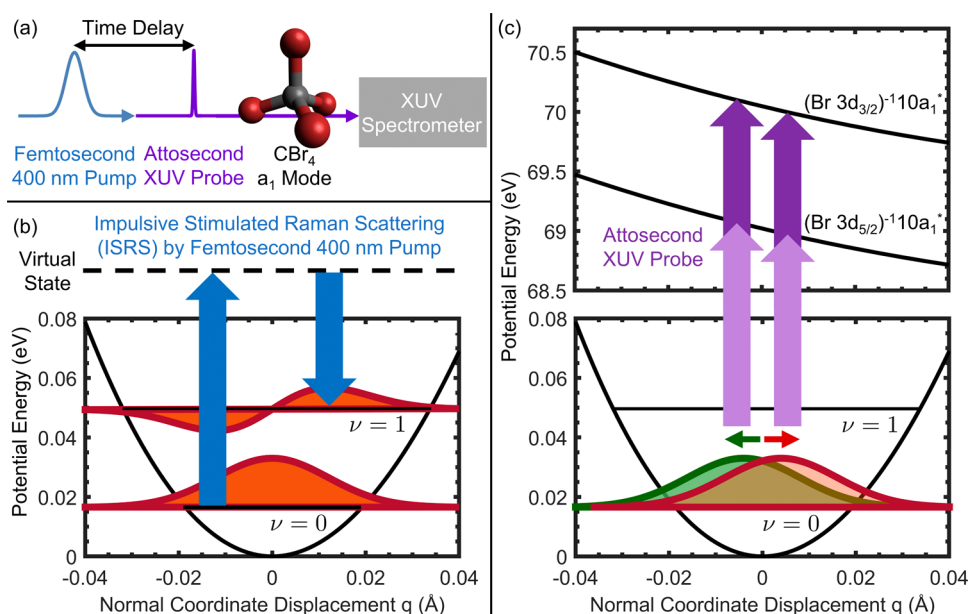
Figure 1. Experimental scheme. (a) Attosecond transient absorption spectroscopy on the symmetric stretch (a_1) mode of CBr_4. (b) Vibrational eigenstates are coherently excited by nonresonant impulsive stimulated Raman scattering (ISRS) with a 400 nm 26 fs pump pulse, and a vibrational wavepacket is launched on the electronic ground state potential energy surface. (c) Vibrational wavepacket dynamics are monitored by time-resolved absorption of attosecond XUV probe pulses (purple arrows) from the electronic ground state to the $(Br\ 3d_{3/2,5/2})^{-1}10a_1{}^*$ electronic core-excited states around 70 eV. The wavepackets drawn in green and red represent the motion shifting toward negative and positive normal mode displacement q, respectively. The wavepacket looks primarily like the vibrational ground state ($\nu = 0$) because only a small fraction of the population in vibrational ground state ($\nu = 0$) is excited to the vibrational first-excited state ($\nu = 1$) by ISRS.

geometry from restricted open-shell Kohn−Sham (ROKS) calculations.[29−31] This slope is used to retrieve the excursion amplitude of the vibrational wavepacket (in terms of C−Br bond-length displacement) and the population transferred by ISRS to the vibrational first-excited state in the small-displacement limit from the measured time-resolved XUV absorption spectrum.

Experimentally, the results show that XUV ATAS is capable of resolving small bond-length changes during vibrational wavepacket dynamics to the order of 10^{-4} Å with femtosecond temporal resolution. Moreover, with analytical formulations, we offer a clear physical picture on multiple levels of understanding of how the pump-pulse peak intensity controls the vibrational dynamics launched by nonresonant ISRS in the small-displacement limit.

2. METHODS

2.1. Experiment. The scheme of attosecond transient absorption spectroscopy on CBr_4, the 400 nm pump pulse, and the XUV probe pulse are briefly outlined here and in Figure 1. The laser source is a Coherent Astrella USP (800 nm, 35 fs fwhm, 7 mJ, 1 kHz), and its output is split by a 70% transmitted and 30% reflected beamsplitter into pump and probe arms, respectively.

2.1.1. 400 nm Pump Pulse. The pump arm starts with 70% of the Astrella output (800 nm, 35 fs fwhm, 4.9 mJ) and undergoes second harmonic generation (SHG) in a β-barium borate (BBO) crystal, and the central wavelength becomes 400 nm. Then it is free-space focused through a Ne-filled (1.7 bar) tube (1.37 m long) to gently broaden the spectrum and then compressed by chirped mirrors. The pulse duration of the main peak in the intensity envelope is measured to be 26 ± 1 fs fwhm by home-built self-diffraction frequency-resolved optical gating (SD-FROG) (Figure S3, Supporting Information).

2.1.2. Few-Cycle Visible-NIR Pulse (Driving Field for High Harmonic Generation). The probe arm starts with 30% of the Astrella output (800 nm, 35 fs fwhm, 2.1 mJ) and is focused into a Ne-filled (2.4 bar) hollow core fiber (HCF) (1.5 m long, 400 μm inner diameter), where it undergoes supercontinuum generation, and then the pulses are compressed by chirped mirrors. After the chirped mirrors, the spectrum spans from around 500 to 900 nm. The dispersion is further fine-tuned by an ADP crystal and a pair of thin glass wedges. The output is few-cycle (∼4 fs) visible-NIR pulses that are used as the driving field for the high harmonic generation (HHG) into the XUV region.

2.1.3. XUV Probe Pulse. The few-cycle visible-NIR pulses (referred to as the driving field) are focused into a Ne gas cell (∼80 mmHg, 300 μm hole diameter), and an XUV probe attosecond pulse train (∼50−85 eV photon energy) (Figure S8, Supporting Information) is produced by high harmonic generation (HHG). The remaining 800 nm driving field is removed by an Al filter (0.1 μm thick).

2.1.4. Static and Time-Resolved (Transient) XUV Absorption Measurement. At the sample cell (4 mm long, 500 μm hole diameter), 400 nm pump and XUV probe beams recombine noncollinearly and interact with CBr_4 vapor. The sample reservoir, delivery line, and cell are heated to 100−120 °C to obtain enough vapor pressure from solid CBr_4. The time delay between the pump and probe pulses is controlled by changing the optical path length between the pump and probe beamlines with a translational stage. After a Zr filter (0.1 μm thick) is used to block the 400 nm beam, the XUV beam is dispersed by a grating and detected on an XUV CCD camera.

Two types of XUV absorption spectra are collected experimentally. One is the static XUV absorbance $A(E_{XUV})$
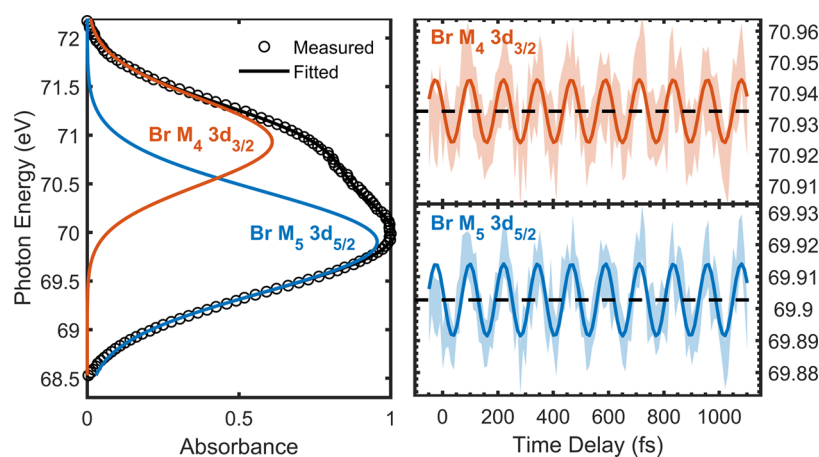
Figure 2. (Left) Static XUV absorption spectrum of CBr_4 at Br $M_{4,5}$ $3d_{3/2,5/2}$ edges from the electronic ground state to the $(Br\ 3d_{3/2,5/2})^{-1}10a_1*$ core-excited states. The spin−orbit doublet is resolved by fitting to a sum of two Voigt functions. The extracted peak energies are 70.932 ± 0.011 and 69.903 ± 0.008 eV for the Br M_4 $3d_{3/2}$ and M_5 $3d_{5/2}$ edges, respectively, with a 1.03 ± 0.01 eV spin−orbit splitting. (Right) Time-resolved XUV absorption spectrum of CBr_4 as a function of time delay between the 400 nm pump and XUV probe pulses. The positive time delay is when the 400 nm pulse arrives before the XUV pulse. The peak intensity of the pump pulse is 20.2×10^{12} W/cm^2. Color shade: extracted peak energy with error bars at each time delay. Solid line: a sine function fitted to the extracted peak energies. The fitted period is 123 ± 1 fs, amplitude 10.2 ± 1.4 meV, and center 70.934 ± 0.001 eV (black dashed line) for the M_4 $3d_{3/2}$ edge, while the M_5 $3d_{5/2}$ edge yields 123 ± 1 fs, 11.3 ± 1.4 meV, and 69.903 ± 0.001 eV (black dashed line). The oscillations for the two edges are almost temporally in phase with a 0.1 ± 0.4 rad phase difference.

$$A(E_{XUV}) = -\log_{10}\frac{I_{XUV}(E_{XUV})}{I_{XUV}^{(0)}(E_{XUV})} \qquad (1)$$

where E_{XUV} is the photon energy of XUV probe pulses, and I_{XUV} and $I_{XUV}^{(0)}$ are the XUV intensity with and without the CBr_4 molecule in the cell, respectively. The other is the time-resolved (transient) XUV differential absorption $\Delta A(E_{XUV}, \tau)$

$$\Delta A(E_{XUV}, \tau) = -\log_{10}\frac{I_{XUV+pump}(E_{XUV}, \tau)}{I_{XUV}(E_{XUV}, \tau)} \qquad (2)$$

where τ is the time delay between the pump and probe pulses, and $I_{XUV+pump}$ and I_{XUV} are the XUV spectrum of CBr_4 with and without the pump pulse.

Temporal resolution is calibrated with a cross-correlation measurement of a 400 nm pump and XUV probe pulses on the He 2s2p state. The fitted instrument response function is 26 ± 6 fs, and the time zero is 1 ± 3 fs. The spectral axis is calibrated with a static XUV absorption spectrum of He 2snp ($n \geq 2$) states. Details are in the Supporting Information.

2.1.5. Pump-Pulse Peak-Intensity Dependent Measurements. The peak intensity of the 400 nm pump pulse is modified by cropping the beam with an iris before the pump and probe pulses recombine. The peak intensity at the sample cell location is estimated to range from 8.1 to 20.2×10^{12} W/cm^2. Detailed calibrations are given in the Supporting Information.

2.2. Calculation. Quantum chemical calculations are performed with the Q-Chem software package,[32] utilizing the SCAN0 functional[33] and the decontracted (i.e., all primitives are uncontracted) aug-cc-pVTZ basis set.[34−36] Scalar relativistic effects are included through the use of the spin-free exact two-component one-electron (SF-X2C-1e) approach.[37−40] Local exchange-correlation integrals are calculated by quadrature over a radial grid with 250 points and an angular Lebedev grid with 974 points. The electronic ground state is modeled with the standard restricted Kohn−Sham procedure,[41] yielding an equilibrium bond distance of 1.925 Å (vs an experimental[42] value of of 1.942 Å) and a symmetric

stretch frequency of 282 cm^{-1} (vs 267 cm^{-1} from experiment[43]).

The isotropic polarizability of the molecule is computed via finite differences of the energy with a five-point stencil (using electric field strengths of 0.005 and 0.01 au, see Supporting Information) over bond lengths ranging from 1.8246 to 2.0246 Å (in increments of 0.001 Å). This polarizability is subsequently utilized to carry out nuclear time-dependent Schrödinger equation simulations of the ISRS process induced by the pump laser pulse and the resulting nuclear dynamics along the symmetric stretching mode, as described in detail in the Supporting Information.

The Br 3d excitation energies are computed with the ROKS approach,[29,30] which has been found to be quite effective at modeling core-level spectroscopies.[31,44] Excited state orbital optimization is carried out with the square gradient minimization algorithm.[45] Spin−orbit effects are subsequently incorporated in the manner described previously.[31] This quasi-degenerate perturbation-theory-based approach constructs a zeroth-order effective Hamiltonian of the spin−orbit free 3d excitation energies at a given geometry, to which a spin−orbit coupling operator $-J\vec{L}\cdot\vec{S}$ is added (where $\vec{S}$ is the electron spin operator and $\vec{L}$ is the orbital angular momentum for d electrons). The coupling constant J is assumed to be constant for all geometries and chosen to be 0.40 eV since this value reproduces the experimentally observed multiplet splitting of 1.03 eV between the $3d_{5/2}$ and $3d_{3/2}$ absorption energies. Core-level excitation energies are computed over bond lengths ranging from 1.9046−1.9446 Å, in increments of 0.001 Å, and are fitted to a straight line against the bond length (see Figure 3) in order to determine the slope of the core-excited PES vs bond elongation.

3. RESULTS AND DISCUSSION

3.1. Detection of the Coherent Vibrational Dynamics: Static and Time-Resolved XUV Absorption Spectrum of CBr_4 at Br $M_{4,5}$ $3d_{3/2,5/2}$ Edge. Figure 2 (left) shows the static XUV absorption spectrum of CBr_4 from the electronic ground

state to the $(Br\ 3d_{3/2,5/2})^{-1}10a_1*$ core-excited states ($10a_1*$ is an unoccupied antibonding orbital[46,47]). The spin−orbit doublet is resolved by fitting the value to a sum of two Voigt functions. The extracted peak energies are 70.932 ± 0.011 and 69.903 ± 0.008 eV for the Br $M_4\ 3d_{3/2}$ and $M_5\ 3d_{5/2}$ edges, respectively (three decimal places are included here to compare with the very small (few to tens of meV) oscillation amplitudes of XUV absorption energy measured and discussed below). The spin−orbit splitting is 1.03 ± 0.01 eV (Table 1).

Table 1. Excitation Energies (eV) of $(Br\ 3d_{3/2,5/2})^{-1}10a_1*$ Core-Excited States in CBr_4

core-excited state	experiment (this work)	ROKS calculations (this work)	previous experiment[46]
$(Br\ 3d_{3/2})^{-1}10a_1*$	70.932 ± 0.011	70.05	70.5
$(Br\ 3d_{5/2})^{-1}10a_1*$	69.903 ± 0.008	69.02	69.6
spin−orbit splitting	1.03 ± 0.01	1.03	0.9

They agree reasonably with previous experimental results[46] (70.5 and 69.6 eV). ROKS calculations yield slightly lower excitation energy values of 70.05 and 69.02 eV, indicating a somewhat larger difference between the theory and the current experiment (∼0.9 eV) than the ∼0.3 eV deviations previously observed for the K- and L-edges of lighter elements.[31,44]

Next, we consider changes to the XUV absorption due to the vibrational wavepacket launched by a 400 nm pump pulse (peak intensity 20.2×10^{12} W/cm^2). In the time-resolved XUV absorption spectrum in Figure 2 (right), when the vibrational wavepacket travels back and forth on the electronic ground state PES, the XUV absorption peak oscillates correspondingly with the vibrational period. The fitted periods are 123 ± 1 fs for both the Br $M_4\ 3d_{3/2}$ edge and $M_5\ 3d_{5/2}$ edge, which agrees with the literature value of 126 fs for the symmetric stretch mode (267 cm^{-1}).[43] The oscillations in the peak position for the two edges are almost temporally in phase with a 0.1 ± 0.4 rad phase difference. Oscillatory behaviors corresponding to the other normal modes of the molecule are not observed (despite such modes being Raman active) because there is no net displacement along such asymmetric modes, as has been observed and discussed in previous work for CCl_4.[28]

If the launching mechanism of the vibrational wavepacket is a pure nonresonant ISRS from a Gaussian pump pulse centered at time zero, the expectation value of the wavepacket position will be a sine function with a zero initial phase.[6,8] Nuclear TDSE simulations reproduce this expectation by retrieving around 0.01 π initial phase of the wavepacket position for all intensities using the temporal intensity envelope of the pump pulse retrieved from SD-FROG (Figure S6). Experimentally, there may be a growing time-zero drift over the course of experiments, and it seems to be reflected in the gradual deviation of the initial phase from zero. As a result, we did not attempt to determine the absolute initial phases from the experiments (Supporting Information).

3.2. Information Encoded in the Time-Resolved XUV Absorption Spectrum: Oscillation Amplitude of XUV Absorption Energy, Excursion Amplitude of Vibrational Wavepacket, and Slope of Core-Excited State Potential Energy Surface. When the vibrational wavepacket results in a normal mode displacement q on the electronic ground state PES $E_g(q)$, the XUV absorption energy $E_{XUV}(q)$ from the electronic ground state to the core-excited state PES $E_{ce}(q)$ is $E_{XUV}(q) = E_{ce}(q) - E_g(q)$. If the pump-pulse peak intensity is

not too strong to induce a large displacement in q, the harmonic approximation holds and the XUV absorption energy $E_{XUV}(q)$ can be approximated by a Taylor series in q

$$E_{XUV}(q) \approx \left[E_{ce}(0) - E_g(0) \right] + \left[\left(\frac{dE_{ce}}{dq} \right)_0 - \cancel{\left(\frac{dE_g}{dq} \right)_0} \right] q$$
$$= E_{XUV}(0) + \left(\frac{dE_{ce}}{dq} \right)_0 q \tag{3}$$

where the slope of the electronic ground state PES $E_g(q)$ vanishes at the ground state equilibrium position $q = 0$, while the slope of the electronic core-excited state PES $E_{ce}(q)$ will generally be nonzero at the Franck−Condon region if the equilibrium position of the core-excited PES does not coincide with that of the ground state.

As the vibrational wavepacket travels between the outer turning point q_{ot} and the inner turning point q_{it} on the electronic ground state PES, the range of XUV absorption peak energies that can be accessed is

$$|E_{XUV}(q_{ot}) - E_{XUV}(q_{it})| = \left| \left(\frac{dE_{ce}}{dq} \right)_0 \right| (q_{ot} - q_{it}) \tag{4}$$

where $\Delta E_{XUV} \equiv |E_{XUV}(q_{ot}) - E_{XUV}(q_{it})|/2$ is defined as the oscillation amplitude of the XUV absorption energy, and $q_{amp} \equiv (q_{ot} - q_{it})/2$, the excursion amplitude of the vibrational wavepacket, or physically the maximum displacement from equilibrium. Therefore

$$\Delta E_{XUV} = \left| \left(\frac{dE_{ce}}{dq} \right)_0 \right| q_{amp} \tag{5}$$

and q_{amp} can thus be retrieved from ΔE_{XUV} in the experimentally measured time-resolved XUV absorption spectrum in Figure 2 (right), if the slope of the core-excited state PES along the normal mode at the electronic ground state equilibrium geometry is known.

In this work, the slope of the $(Br\ 3d_{3/2,5/2})^{-1}10a_1*$ core-excited states PES is calculated from ROKS to be approximately −9.4 eV/Å along the symmetric stretch mode (by fitting core-excitation energies to a straight line, as shown in Figure 3). In other words, this slope suggests that the Br $3d_{3/2,5/2} \rightarrow 10a_1*$ excitation energy decreases by 9.4 eV as the C−Br bond length increases by 1 Å. This is consistent with the antibonding character of the $10a_1*$ orbital, as the energy of this state should significantly decrease with bond elongation. This 9.4 eV/Å value for the slope is on the same order of magnitude (∼10 eV/Å) as previous estimates for core-to-antibonding excitations in CCl_4[28] and SF_6[26,27] (typical range 5−30 eV/Å depending on which atom).

The ROKS results and the linear fits are shown in Figure 3, which indicates that eq 3 holds quite well for bond stretches as high as ±0.05 Å relative to equilibrium and higher order effects do not appear to be relevant in this regime. Around 10 meV or smaller experimental oscillation amplitudes of XUV absorption energies (Figure 2) and the computed slope −9.4 eV/Å collectively indicate that the bond stretches remain on the order of 10^{-4} to 10^{-3} Å, and the linear behavior reported in eq 3 therefore is sufficient for analyzing the experimental results.

3.3. Relative Slope between Multiple Core-Excited State PES and Insight into Property of Participating Orbitals. If multiple electronic core-excited states simulta-
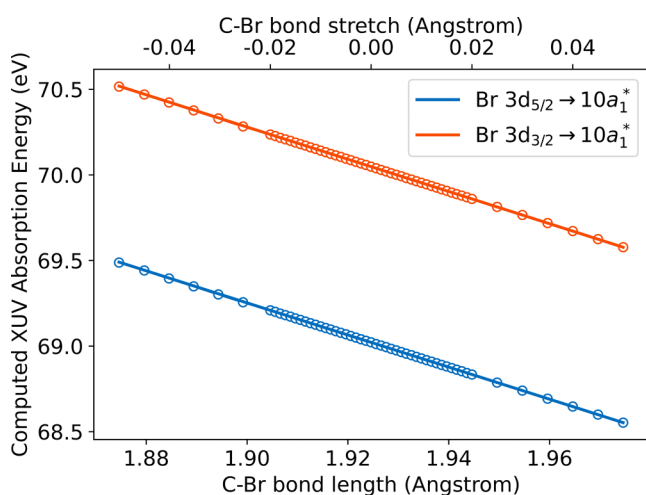
Figure 3. Computed XUV absorption energies from ROKS along the symmetric stretch a_1 normal mode as a function of C−Br bond length (open circles) around the equilibrium geometry (1.925 Å). The linear fits obtained from fitting to ROKS results for 41 equally spaced bond lengths between 1.9046 and 1.9446 Å are also shown (solid lines), which align quite well with ROKS results for 12 bond lengths calculated outside the fit interval (six equally spaced points each between 1.8746 and 1.8996 and 1.9496 and 1.9746 Å). The slopes are about −9.4 eV/Å for the Br $3d_{3/2,5/2} \rightarrow 10a_1^*$ excitations.

neously probe the vibrational wavepacket on the electronic ground state, the relative slope between two or more core-excited state PESs[26−28] along the normal mode at the equilibrium geometry of the electronic ground state can be determined experimentally, from the ratio of the measured oscillation amplitude of XUV absorption energy ΔE_{XUV} using eq 5 as

$$\left|\left(\frac{dE_{ce2}}{dq}\right)_0\right| \Big/ \left|\left(\frac{dE_{ce1}}{dq}\right)_0\right| = \Delta E_{XUV2}/\Delta E_{XUV1} \quad (6)$$

because here the excursion amplitude of the vibrational wavepacket q_{amp} is the same. In this work, the relative slope between the two (Br $3d_{3/2,5/2})^{-1}10a_1^*$ core-excited states PES is determined experimentally to be 1.1 ± 0.13 as the ratio of the measured oscillation amplitude of XUV absorption energy ΔE_{XUV} (Br $3d_{5/2})/\Delta E_{XUV}$ (Br $3d_{3/2}$) (Table S4, Supporting Information). As a result, the shapes of the two core-excited state PESs are quite similar around the equilibrium geometry of the electronic ground state.

Such relative slopes not only offer experimental information on the shape of core-excited state PES but also shed light on the nature of the participating orbitals. For the discussion below, a core-excited state is approximated as a singly excited electronic configuration, where one electron is excited from an initial core orbital to a final orbital that is higher in energy.

One scenario is when the electron is excited from the same core orbital to different final orbitals. The relative slopes of the corresponding core-excited state PESs belonging to the same absorption edge give a hint about the bonding properties of the final orbitals. For instance, if the final orbital is nonbonding, then the resulting core-excited state will be generally less sensitive to changes in the molecular geometry, and its PES will be relatively flat. As a result, its slope will be smaller than the slope of other core-excited states PES where the final orbital is bonding or antibonding. For instance, in the SF_6

molecule,[26,27] an electron can be excited from S 2p core orbital to three different final orbitals a_{1g}, t_{2g}, and e_g. Because the a_{1g} and e_g orbitals are antibonding while the t_{2g} orbital is nonbonding, the slope of (S 2p)$^{-1}a_{1g}$ and (S 2p)$^{-1}e_g$ core-excited states is found to be larger than that of the (S 2p)$^{-1}t_{2g}$ state.

The other scenario is when the electron is excited from different core orbitals to the same final orbital or the corresponding core-excited states originate from different absorption edges. This offers a possible way to compare different core orbitals on the same atom or core orbitals on different atoms in a molecule. In this work, the electron is excited to the same $10a_1^*$ antibonding orbital, but from different Br $3d_{3/2}$ or Br $3d_{5/2}$ core orbitals, corresponding to the Br M_4 or M_5 absorption edges. The ratio of slopes of these two core-excited states is close to unity as mentioned above, indicating that both Br $3d_{3/2}$ and Br $3d_{5/2}$ core orbitals respond similarly to the bond-length change. This is reasonable, as these two core orbitals come from the same set of Br 3d orbitals, split by spin−orbit coupling. On the other hand, a previous study on CCl_4 molecule[28] found the slope for the (Cl $2p_{3/2})^{-1}8t_2^*$ core-excited state to be much larger than that of the (C 1s)$^{-1}8t_2^*$ core-excited state, despite the same final orbital ($8t_2^*$) for both excitations.

3.4. Connection between the Excursion Amplitude of Vibrational Wavepacket and Vibrational Eigenstate Populations, in the Small-Displacement Limit. In the small-displacement limit, only the vibrational ground ψ_0 and first-excited ψ_1 states of a harmonic oscillator need to be considered.[26] Long after the pump pulse, the coherent vibrational wavepacket $\Psi(q, t)$ can be approximated by the following linear superposition,

$$\Psi(q, t) = c_0\psi_0(q)e^{-iE_0t/\hbar} + c_1\psi_1(q)e^{-iE_1t/\hbar} \quad (7)$$

where q is the normal mode displacement (position) and $E_{0,1}$ is the vibrational energy of the vibrational ground and first-excited states, respectively. The expectation value of position $\langle q(t) \rangle$ of this vibrational wavepacket is

$$\langle q(t) \rangle$$
$$= \langle \Psi(q, t)|q|\Psi(q, t) \rangle$$
$$= p_0\langle\psi_0|q|\psi_0\rangle + p_1\langle\psi_1|q|\psi_1\rangle$$
$$\quad + 2\sqrt{p_0 p_1}\langle\psi_0|q|\psi_1\rangle\cos[(E_1 - E_0)t/\hbar + \phi] \quad (8)$$

where $p_{0,1} = |c_{0,1}|^2$ is the population of the vibrational ground and first-excited states, respectively, and ϕ is the initial phase between the two coefficients $c_{0,1}$. (If the launching mechanism of the coherent vibrational wavepacket is nonresonant ISRS from a Gaussian pump pulse centered at time zero, the expectation value of position $\langle q(t) \rangle$ will be a sine function with a zero initial phase,[6,8] or equivalently a cosine function with a $-\pi/2$ initial phase in eq 8).

Next, because $\langle\psi_0|q|\psi_0\rangle = \langle\psi_1|q|\psi_1\rangle = 0$ and $\langle\psi_0|q|\psi_1\rangle = \sqrt{\frac{\hbar}{2\mu\omega_0}}$ for a harmonic oscillator (where μ is the mass associated with the normal mode, which is four times the mass of Br, and $\omega_0 = (E_1 - E_0)/\hbar$ is the fundamental vibrational frequency of the normal mode), the position expectation value simplifies to

$$\langle q(t) \rangle = \left(2\sqrt{p_0 p_1} \sqrt{\frac{\hbar}{2\mu\omega_0}} \right) \cos(\omega_0 t + \phi)$$

$$= \left(2\sqrt{(1-p_1)p_1} \sqrt{\frac{\hbar}{2\mu\omega_0}} \right) \cos(\omega_0 t + \phi)$$

$$= q_{\text{amp}} \cos(\omega_0 t + \phi) \tag{9}$$

as $p_1 + p_0 = 1$. This shows that the excursion amplitude of the vibrational wavepacket is

$$q_{\text{amp}} = 2\sqrt{(1-p_1)p_1} \sqrt{\frac{\hbar}{2\mu\omega_0}} \tag{10}$$

Furthermore, when $p_1 \ll 1$ (as expected in the small-displacement limit),

$$\boxed{q_{amp} \approx 2\sqrt{p_1} \sqrt{\frac{\hbar}{2\mu\omega_0}}} \tag{11}$$

so q_{amp} is proportional to $\sqrt{p_1}$. Therefore, if the excursion amplitude of the vibrational wavepacket is known, then the population in the vibrational first-excited state can be determined from this relation.

The validity of the above formulation is also verified against numerical simulations of the nuclear time-dependent Schrödinger equation (TDSE) along the symmetric stretch mode alone. As shown in Figure 4, the calculated population of the
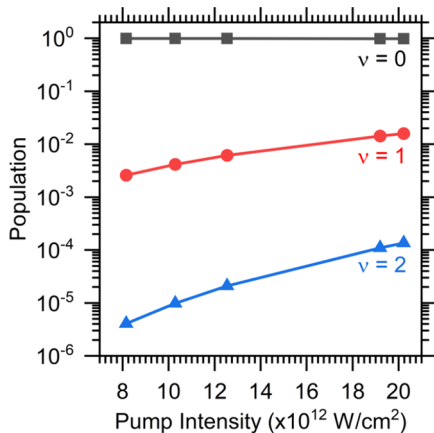
Figure 4. Calculated populations of the vibrational eigenstates ($\nu = 0$, 1, 2) of the symmetric stretch a_1 mode from nuclear TDSE simulations, as a function of the experimental 400 nm pump-pulse peak intensity. The population of the vibrational first-excited state remains small (around the order of 10^{-3}). This shows that the pump light–matter interaction is in the small-displacement limit for the range of pump-pulse peak intensities used in this work. The population in the vibrational second-excited state is even smaller (around the order of 10^{-5}), indicating that the two-state approximation is reasonable as well.

vibrational ground state is close to one (on the order of 0.99), and the calculated population of the vibrational first-excited state is indeed small (around the order of 10^{-3}) for the pump pulse intensities used in this work. As a result, the pump light–matter interaction studied in this work is clearly in the small-displacement limit. Furthermore, the population in the vibrational second-excited state is even smaller (around the

order of 10^{-5}), indicating that the two-state approximation is reasonable as well.

3.5. Physical Basis for the Phenomenological Equations in the Literature to Fit the Oscillations in Time-Resolved XUV Absorption Spectrum due to Coherent Vibrational Dynamics. Based on the formulation above, a physical basis can be provided for the phenomenological equations that have often been used in the literature,[9,12,14,23,24,27] to fit the oscillations in time-resolved XUV absorption spectrum due to coherent vibrational dynamics. For instance, if one vibrational mode is involved, the time-resolved XUV absorption energy is often described empirically as

$$E_{\text{XUV}}(t) = E^0_{\text{XUV}} + \Delta E_{\text{XUV}} \cos(\omega_0 t + \phi) \tag{12}$$

where E^0_{XUV} is the XUV absorption energy at the equilibrium geometry of the electronic ground state and ΔE_{XUV} is the oscillation amplitude of XUV absorption energy. Comparing to eq 5,

$$\Delta E_{\text{XUV}} = \left| \left(\frac{dE_{\text{ce}}}{dq} \right)_0 \right| q_{\text{amp}} \tag{5}$$

it further reveals that the oscillation amplitude of XUV absorption energy ΔE_{XUV} is proportional to the slope of core-excited state PES along the normal mode at the electronic ground state equilibrium geometry and the excursion amplitude of vibrational wavepacket q_{amp}, within the harmonic approximation.

For example, larger amplitudes can thus result from steeper slopes of the core-excited PES (which can be attained through excitation to an antibonding orbital, as in this work) or from higher pump-pulse peak intensity to access greater excursion amplitudes of vibrational wavepacket q_{amp}, by adding a larger fraction of the vibrational first-excited state in the small-displacement limit.

3.6. Controlling the Motion of Vibrational Wavepacket with Different Pump-Pulse Peak Intensities in the Small-Displacement Regime. The dynamics of the vibrational wavepackets are initiated with five different pump-pulse peak intensities ranging from 8.1 to 20.2×10^{12} W/cm^2 (detailed calibrations are shown in Table S1). In Figure 5a, the experimentally measured oscillation amplitudes of XUV absorption energy ΔE_{XUV} increase approximately linearly with pump-pulse peak intensity, which is also observed for the SF$_6$ molecule.[26,27]

In Figure 5b, the excursion amplitudes of the vibrational wavepacket q_{amp} are retrieved from the corresponding oscillation amplitudes of the XUV absorption energy ΔE_{XUV} by eq 5, given the −9.4 eV/Å slope of the $(\text{Br } 3d_{3/2,5/2})^{-1}10a_1^*$ core-excited state PES from ROKS calculations. In Figure 5c, the square root of the population in the vibrational first-excited state $\sqrt{p_1}$ is further estimated from the excursion amplitude of the vibrational wavepacket q_{amp} via eq 11. As expected, all three quantities plotted in Figure 5 are found to increase approximately linearly with the pump-pulse peak intensity for the Br M_4 $3d_{3/2}$ and M_5 $3d_{5/2}$ edges.

The experimentally measured and retrieved values are also compared with nuclear TDSE simulations. The theoretical population of the vibrational first-excited state p_1 and excursion amplitude of the vibrational wavepacket q_{amp} come from numerically solving the nuclear TDSE for the nonresonant ISRS process, and the theoretical oscillation amplitude of XUV
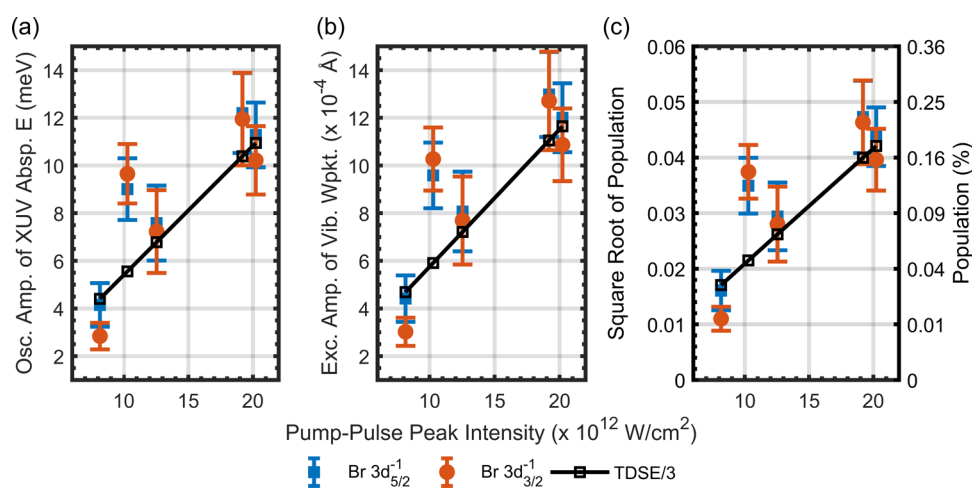
Figure 5. Pump-pulse peak-intensity dependence of (a) experimentally measured oscillation amplitude of the XUV absorption energy ΔE_{XUV}, (b) excursion amplitude of the vibrational wavepacket q_{amp} (retrieved from (a) by eq 5, given the -9.4 eV/Å slope of the (Br $3d_{3/2,5/2}$)$^{-1}10a_1^*$ core-excited state PES from ROKS calculations), and (c) square root of the population transferred to the vibrational first-excited state $\sqrt{p_1}$ (estimated from (b) by eq 11). All three quantities increase approximately linearly with the pump-pulse intensity for both the Br M_4 $3d_{3/2}$ (orange circle) and M_5 $3d_{5/2}$ (blue square) edges. Estimates of all three quantities from nuclear TDSE simulations (black open square) for the ISRS process are also provided (scaled by 1/3, see text for details) and show clear linear relationships with the pump-pulse intensities used in this work. The outlier at 10.3×10^{12} W/cm^2 may result from the fluctuation in average power measurement, as the average power is close to the lower limit of the working range for the power meter head (Coherent PowerMax PM10).

absorption energy ΔE_{XUV} is estimated from eq 5. The TDSE simulation results are scaled by 1/3 to match the experiment. A few possible reasons for this discrepancy between experiment and theory are considered below.

From an experimental perspective, the differences with theory may arise from a lower effective pump-pulse peak intensity at the sample location than in the estimation. A detailed calibration of the experimental peak intensity for the pump pulse is given in the Supporting Information, which is taken as our best estimation. However, it is uncertain how precise the pump and probe pulses spatially overlap at the beam center of each other. If the spatial overlap is off-center, the effective pump-pulse peak intensity within the probe beam area will become smaller. Before the measurements on CBr$_4$, the spatial overlap was confirmed by overlapping the recombined pump beam and the HHG driving-field beam on a beam profiler at a location with equivalent distance to the sample cell, as the XUV probe beam most likely follows the same path of the HHG driving-field beam. On the other hand, the outlier at 10.3×10^{12} W/cm^2 may result from the fluctuations in average power measurement, as the average power is close to the lower limit of the working range for the power meter head (Coherent PowerMax PM10).

Potential computational origins of this discrepancy are errors in the Br 3d core-excited PES slope value of -9.4 eV/Å, or inadequacies in modeling the nonresonant ISRS process through TDSE (such as from errors in the molecular polarizabilities). We consider these factors to be somewhat less likely, as the slope is quite consistent with previous results for other molecules,[28] and additional effort has been invested into benchmarking molecular polarizabilities used for the TDSE simulations (see Supporting Information). We note that the TDSE simulations account for rotational averaging effects on the interaction between the molecule and the pump-pulse field through the use of isotropic polarizability.

4. CONCLUSIONS

In this work, a coherent vibrational wavepacket is launched in the symmetric stretching (a_1) mode of the electronic ground state CBr$_4$ molecule by nonresonant impulsive stimulated Raman scattering (ISRS) with 400 nm pump pulses. Dynamics of this vibrational wavepacket are studied with time-resolved absorption of attosecond XUV pulses at the bromine $M_{4,5}$ $3d_{3/2,5/2}$ edges around 70 eV, with excitations to the lowest energy antibonding ($10a_1^*$) orbital. The measured XUV absorption energies oscillate in time with the period of the symmetric stretching mode (123 ± 1 fs), and the oscillation amplitude of the XUV absorption energy equals the product of the excursion amplitude of the vibrational wavepacket and the slope of the (Br $3d_{3/2,5/2}$)$^{-1}10a_1^*$ core-excited state potential energy surface along this mode. Since the measured oscillation amplitude of XUV absorption energy is on the order of few to tens of meV and the slope is -9.4 eV/Å from ROKS calculations, the excursion amplitude of the vibrational wavepacket (C−Br bond-length displacement) is retrieved to be on the order of 10^{-4} to 10^{-3} Å. Harmonic approximation therefore holds quite well in this small-displacement limit.

Experiments with various pump-pulse peak intensities ($8.1-20.2 \times 10^{12}$ W/cm^2) show an approximately linear relationship between the intensity and the measured oscillation amplitude of XUV absorption energy, and between the intensity and the retrieved excursion amplitude of vibrational wavepacket as well. Furthermore, the excursion amplitude of the vibrational wavepacket is proportional to the square root of the population in the vibrational first-excited state in the small-displacement limit. This relation enables an indirect estimate of this population from the measured oscillation amplitude of XUV absorption energy. These linear relationships are supported by analytical formulations and numerical simulations of the nuclear time-dependent Schrödinger equation along the symmetric stretching mode for the nonresonant ISRS.

The present analytical formulations and approaches to extract information encoded in time-resolved XUV absorption

spectra are general and can be readily applied to ISRS combined with other time-resolved electronic absorption spectroscopy probed in different spectral regions. Experimentally, the results show that XUV attosecond transient absorption spectroscopy is capable of resolving the small bond-length changes during vibration with extraordinary 10^{-4} to 10^{-3} Å and tens of femtosecond precision.[26] Moreover, the analytical formulations provide a concrete and thorough understanding of how the pump-pulse peak intensity controls the vibrational dynamics in the small-displacement limit.

ASSOCIATED CONTENT

Supporting Information

The Supporting Information is available free of charge at https://pubs.acs.org/doi/10.1021/acs.jpca.4c05210.

> Calibration of pump pulse (beam diameter, average power, peak intensity, and self-diffraction frequency-resolved optical gating (SD-FROG) measurement) (1); calibration of time zero and temporal resolution for time-resolved XUV absorption measurements (2); calibration of the spectral axis (3); measured relative slope of Br 3d core-excited state potential energy surface (PES) (4); comment about the initial phase of wavepacket trajectory (5); nuclear time-dependent Schrödinger equation simulations (6); and comment about polarizability calculations (7) (PDF)
>
> TDSE code and calculated potential energy surface and polarizability of CBr_4 (ZIP)

AUTHOR INFORMATION

Corresponding Author

Stephen R. Leone − *Department of Chemistry, University of California, Berkeley, California 94720, United States; Chemical Sciences Division, Lawrence Berkeley National Laboratory, Berkeley, California 94720, United States; Department of Physics, University of California, Berkeley, California 94720, United States;* orcid.org/0000-0003-1819-1338; Email: srl@berkeley.edu

Authors

Jen-Hao Ou − *Department of Chemistry, University of California, Berkeley, California 94720, United States;* orcid.org/0000-0002-5978-6381

Diptarka Hait − *Department of Chemistry and The PULSE Institute, Stanford University, Stanford, California 94305, United States; SLAC National Accelerator Laboratory, Menlo Park, California 94024, United States;* orcid.org/0000-0003-1570-920X

Patrick Rupprecht − *Department of Chemistry, University of California, Berkeley, California 94720, United States; Chemical Sciences Division, Lawrence Berkeley National Laboratory, Berkeley, California 94720, United States*

John E. Beetar − *Department of Chemistry, University of California, Berkeley, California 94720, United States; Present Address: NSF National eXtreme Ultrafast Science (NeXUS) Facility, Columbus, Ohio 43210, United States*

Todd J. Martínez − *Department of Chemistry and The PULSE Institute, Stanford University, Stanford, California 94305, United States; SLAC National Accelerator Laboratory, Menlo Park, California 94024, United States;* orcid.org/0000-0002-4798-8947

Complete contact information is available at:

https://pubs.acs.org/10.1021/acs.jpca.4c05210

Notes

The authors declare no competing financial interest.

ACKNOWLEDGMENTS

REFERENCES

(1) Ohmori, K. Wave-Packet and Coherent Control Dynamics. *Annu. Rev. Phys. Chem.* **2009**, *60* (1), 487−511.

(2) Townsend, D.; Sussman, B. J.; Stolow, A. A Stark Future for Quantum Control. *J. Phys. Chem. A* **2011**, *115* (4), 357−373.

(3) Goulielmakis, E.; Loh, Z.-H.; Wirth, A.; Santra, R.; Rohringer, N.; Yakovlev, V. S.; Zherebtsov, S.; Pfeifer, T.; Azzeer, A. M.; Kling, M. F.; Leone, S. R.; Krausz, F. Real-Time Observation of Valence Electron Motion. *Nature* **2010**, *466* (7307), 739−743.

(4) Geneaux, R.; Marroux, H. J. B.; Guggenmos, A.; Neumark, D. M.; Leone, S. R. Transient Absorption Spectroscopy Using High Harmonic Generation: A Review of Ultrafast X-Ray Dynamics in Molecules and Solids. *Philos. Trans. R. Soc., A* **2019**, *377* (2145), No. 20170463.

(5) Kobayashi, Y.; Leone, S. R. Characterizing Coherences in Chemical Dynamics with Attosecond Time-Resolved x-Ray Absorption Spectroscopy. *J. Chem. Phys.* **2022**, *157* (18), No. 180901.

(6) Yan, Y. X.; Gamble, E. B.; Nelson, K. A. Impulsive Stimulated Scattering: General Importance in Femtosecond Laser Pulse Interactions with Matter, and Spectroscopic Applications. *J. Chem. Phys.* **1985**, *83* (11), 5391−5399.

(7) Ruhman, S.; Joly, A. G.; Nelson, K. A. Coherent Molecular Vibrational Motion Observed in the Time Domain Through Impulsive Stimulated Raman Scattering. *IEEE J. Quantum Electron.* **1988**, *24* (2), 460−469.

(8) Dhar, L.; Rogers, J. A.; Nelson, K. A. Time-Resolved Vibrational Spectroscopy in the Impulsive Limit. *Chem. Rev.* **1994**, *94* (1), 157−193.

(9) Hosler, E. R.; Leone, S. R. Characterization of Vibrational Wave Packets by Core-Level High-Harmonic Transient Absorption Spectroscopy. *Phys. Rev. A* **2013**, *88* (2), No. 023420.

(10) Pertot, Y.; Schmidt, C.; Matthews, M.; Chauvet, A.; Huppert, M.; Svoboda, V.; Von Conta, A.; Tehlar, A.; Baykusheva, D.; Wolf, J.-P.; Wörner, H. J. Time-Resolved x-Ray Absorption Spectroscopy with a Water Window High-Harmonic Source. *Science* **2017**, *355* (6322), 264−267.

(11) Warrick, E. R.; Bækhøj, J. E.; Cao, W.; Fidler, A. P.; Jensen, F.; Madsen, L. B.; Leone, S. R.; Neumark, D. M. Attosecond Transient Absorption Spectroscopy of Molecular Nitrogen: Vibrational Coherences in the B′ $^1\sum_u^+$ State. *Chem. Phys. Lett.* **2017**, *683*, 408−415.

(12) Wei, Z.; Li, J.; Wang, L.; See, S. T.; Jhon, M. H.; Zhang, Y.; Shi, F.; Yang, M.; Loh, Z.-H. Elucidating the Origins of Multimode Vibrational Coherences of Polyatomic Molecules Induced by Intense Laser Fields. *Nat. Commun.* **2017**, *8* (1), No. 735.

(13) Wei, Z.; Tian, L.; Li, J.; Lu, Y.; Yang, M.; Loh, Z. H. Tracking Ultrafast Bond Dissociation Dynamics at 0.1 Å Resolution by Femtosecond Extreme Ultraviolet Absorption Spectroscopy. *J. Phys. Chem. Lett.* **2018**, *9* (19), 5742−5747.

(14) Wei, Z.; Li, J.; Zhang, H.; Lu, Y.; Yang, M.; Loh, Z.-H. Ultrafast Dissociative Ionization and Large-Amplitude Vibrational Wave Packet Dynamics of Strong-Field-Ionized Di-Iodomethane. *J. Chem. Phys.* **2019**, *151* (21), No. 214308.

(15) Saito, N.; Sannohe, H.; Ishii, N.; Kanai, T.; Kosugi, N.; Wu, Y.; Chew, A.; Han, S.; Chang, Z.; Itatani, J. Real-Time Observation of Electronic, Vibrational, and Rotational Dynamics in Nitric Oxide with Attosecond Soft x-Ray Pulses at 400 eV. *Optica* **2019**, *6* (12), 1542−1546.

(16) Timmers, H.; Zhu, X.; Li, Z.; Kobayashi, Y.; Sabbar, M.; Hollstein, M.; Reduzzi, M.; Martínez, T. J.; Neumark, D. M.; Leone, S. R. Disentangling Conical Intersection and Coherent Molecular Dynamics in Methyl Bromide with Attosecond Transient Absorption Spectroscopy. *Nat. Commun.* **2019**, *10* (1), No. 3133.

(17) Kobayashi, Y.; Neumark, D. M.; Leone, S. R. Attosecond XUV Probing of Vibronic Quantum Superpositions in Br_2^+. *Phys. Rev. A* **2020**, *102* (5), No. 051102.

(18) Kobayashi, Y.; Chang, K. F.; Poullain, S. M.; Scutelnic, V.; Zeng, T.; Neumark, D. M.; Leone, S. R. Coherent Electronic-Vibrational Dynamics in Deuterium Bromide Probed via Attosecond Transient-Absorption Spectroscopy. *Phys. Rev. A* **2020**, *101* (6), No. 063414.

(19) Zinchenko, K. S.; Ardana-Lamas, F.; Seidu, I.; Neville, S. P.; Van Der Veen, J.; Lanfaloni, V. U.; Schuurman, M. S.; Wörner, H. J. Sub-7-fs Conical-Intersection Dynamics Probed at the Carbon K-Edge. *Science* **2021**, *371* (6528), 489−494.

(20) Rott, F.; Reduzzi, M.; Schnappinger, T.; Kobayashi, Y.; Chang, K. F.; Timmers, H.; Neumark, D. M.; de Vivie-Riedle, R.; Leone, S. R. Ultrafast Strong-Field Dissociation of Vinyl Bromide: An Attosecond Transient Absorption Spectroscopy and Non-Adiabatic Molecular Dynamics Study. *Struct. Dyn.* **2021**, *8* (3), No. 034104.

(21) Loh, Z.-H. Studies of Ultrafast Molecular Dynamics by Femtosecond Extreme Ultraviolet Absorption Spectroscopy. *Chem. Lett.* **2021**, *50* (5), 965−973.

(22) Poullain, S. M.; Kobayashi, Y.; Chang, K. F.; Leone, S. R. Visualizing Coherent Vibrational Motion in the Molecular Iodine B $^3\Pi_{0_u^+}$ State Using Ultrafast XUV Transient-Absorption Spectroscopy. *Phys. Rev. A* **2021**, *104* (2), No. 022817.

(23) Chang, K. F.; Wang, H.; Poullain, S. M.; Prendergast, D.; Neumark, D. M.; Leone, S. R. Mapping Wave Packet Bifurcation at a Conical Intersection in CH3I by Attosecond XUV Transient Absorption Spectroscopy. *J. Chem. Phys.* **2021**, *154* (23), No. 234301.

(24) Chang, K. F.; Wang, H.; Poullain, S. M.; González-Vázquez, J.; Bañares, L.; Prendergast, D.; Neumark, D. M.; Leone, S. R. Conical Intersection and Coherent Vibrational Dynamics in Alkyl Iodides Captured by Attosecond Transient Absorption Spectroscopy. *J. Chem. Phys.* **2022**, *156* (11), No. 114304.

(25) Matselyukh, D. T.; Despré, V.; Golubev, N. V.; Kuleff, A. I.; Wörner, H. J. Decoherence and Revival in Attosecond Charge Migration Driven by Non-Adiabatic Dynamics. *Nat. Phys.* **2022**, *18* (10), 1206−1213.

(26) Rupprecht, P.; Aufleger, L.; Heinze, S.; Magunia, A.; Ding, T.; Rebholz, M.; Amberg, S.; Mollov, N.; Henrich, F.; Haverkort, M. W.; Ott, C.; Pfeifer, T. Resolving Vibrations in a Polyatomic Molecule with Femtometer Precision via X-Ray Spectroscopy. *Phys. Rev. A* **2023**, *108* (3), No. 032816.

(27) Barreau, L.; Ross, A. D.; Kimberg, V.; Krasnov, P.; Blinov, S.; Neumark, D. M.; Leone, S. R. Core-Excited States of SF_6 Probed with Soft-x-Ray Femtosecond Transient Absorption of Vibrational Wave Packets. *Phys. Rev. A* **2023**, *108* (1), No. 012805.

(28) Ross, A. D.; Hait, D.; Scutelnic, V.; Neumark, D. M.; Head-Gordon, M.; Leone, S. R. Measurement of Coherent Vibrational Dynamics with X-Ray Transient Absorption Spectroscopy Simultaneously at the Carbon K- and Chlorine $L_{2,3}$-Edges. *Commun. Phys.* **2024**, *7*, 304.

(29) Frank, I.; Hutter, J.; Marx, D.; Parrinello, M. Molecular Dynamics in Low-Spin Excited States. *J. Chem. Phys.* **1998**, *108* (10), 4060−4069.

(30) Kowalczyk, T.; Tsuchimochi, T.; Chen, P.-T.; Top, L.; Van Voorhis, T. Excitation Energies and Stokes Shifts from a Restricted Open-Shell Kohn-Sham Approach. *J. Chem. Phys.* **2013**, *138* (16), No. 164101.

(31) Hait, D.; Head-Gordon, M. Highly Accurate Prediction of Core Spectra of Molecules at Density Functional Theory Cost: Attaining Sub-Electronvolt Error from a Restricted Open-Shell Kohn−Sham Approach. *J. Phys. Chem. Lett.* **2020**, *11* (3), 775−786.

(32) Epifanovsky, E.; Gilbert, A. T. B.; Feng, X.; Lee, J.; Mao, Y.; Mardirossian, N.; Pokhilko, P.; White, A. F.; Coons, M. P.; Dempwolff, A. L.; Gan, Z.; Hait, D.; Horn, P. R.; Jacobson, L. D.; Kaliman, I.; Kussmann, J.; Lange, A. W.; Lao, K. U.; Levine, D. S.; Liu, J.; McKenzie, S. C.; Morrison, A. F.; Nanda, K. D.; Plasser, F.; Rehn, D. R.; Vidal, M. L.; You, Z.-Q.; Zhu, Y.; Alam, B.; Albrecht, B. J.; Aldossary, A.; Alguire, E.; Andersen, J. H.; Athavale, V.; Barton, D.; Begam, K.; Behn, A.; Bellonzi, N.; Bernard, Y. A.; Berquist, E. J.; Burton, H. G. A.; Carreras, A.; Carter-Fenk, K.; Chakraborty, R.; Chien, A. D.; Closser, K. D.; Cofer-Shabica, V.; Dasgupta, S.; De Wergifosse, M.; Deng, J.; Diedenhofen, M.; Do, H.; Ehlert, S.; Fang, P.-T.; Fatehi, S.; Feng, Q.; Friedhoff, T.; Gayvert, J.; Ge, Q.; Gidofalvi, G.; Goldey, M.; Gomes, J.; González-Espinoza, C. E.; Gulania, S.; Gunina, A. O.; Hanson-Heine, M. W. D.; Harbach, P. H. P.; Hauser, A.; Herbst, M. F.; Hernández Vera, M.; Hodecker, M.; Holden, Z. C.; Houck, S.; Huang, X.; Hui, K.; Huynh, B. C.; Ivanov, M.; Jász, Á.; Ji, H.; Jiang, H.; Kaduk, B.; Kähler, S.; Khistyaev, K.; Kim, J.; Kis, G.; Klunzinger, P.; Koczor-Benda, Z.; Koh, J. H.; Kosenkov, D.; Koulias, L.; Kowalczyk, T.; Krauter, C. M.; Kue, K.; Kunitsa, A.; Kus, T.; Ladjánszki, I.; Landau, A.; Lawler, K. V.; Lefrancois, D.; Lehtola, S.; Li, R. R.; Li, Y.-P.; Liang, J.; Liebenthal, M.; Lin, H.-H.; Lin, Y.-S.; Liu, F.; Liu, K.-Y.; Loipersberger, M.; Luenser, A.; Manjanath, A.; Manohar, P.; Mansoor, E.; Manzer, S. F.; Mao, S.-P.; Marenich, A. V.; Markovich, T.; Mason, S.; Maurer, S. A.; McLaughlin, P. F.; Menger, M. F. S. J.; Mewes, J.-M.; Mewes, S. A.; Morgante, P.; Mullinax, J. W.; Oosterbaan, K. J.; Paran, G.; Paul, A. C.; Paul, S. K.; Pavošević, F.; Pei, Z.; Prager, S.; Proynov, E. I.; Rák, Á.; Ramos-Cordoba, E.; Rana, B.; Rask, A. E.; Rettig, A.; Richard, R. M.; Rob, F.; Rossomme, E.; Scheele, T.; Scheurer, M.; Schneider, M.; Sergueev, N.; Sharada, S. M.; Skomorowski, W.; Small, D. W.; Stein, C. J.; Su, Y.-C.; Sundstrom, E. J.; Tao, Z.; Thirman, J.; Tornai, G. J.; Tsuchimochi, T.; Tubman, N. M.; Veccham, S. P.; Vydrov, O.; Wenzel, J.; Witte, J.; Yamada, A.; Yao, K.; Yeganeh, S.; Yost, S. R.; Zech, A.; Zhang, I. Y.; Zhang, X.; Zhang, Y.; Zuev, D.; Aspuru-Guzik, A.; Bell, A. T.; Besley, N. A.; Bravaya, K. B.; Brooks, B. R.; Casanova, D.; Chai, J.-D.; Coriani, S.; Cramer, C. J.; Cserey, G.; DePrince, A. E.; DiStasio, R. A.; Dreuw, A.; Dunietz, B. D.; Furlani, T. R.; Goddard, W. A.; Hammes-Schiffer, S.; Head-Gordon, T.; Hehre, W. J.; Hsu, C.-P.; Jagau, T.-C.; Jung, Y.; Klamt, A.; Kong, J.; Lambrecht, D. S.; Liang, W.; Mayhall, N. J.; McCurdy, C. W.; Neaton, J. B.; Ochsenfeld, C.; Parkhill, J. A.; Peverati, R.; Rassolov, V. A.; Shao, Y.; Slipchenko, L. V.; Stauch, T.; Steele, R. P.; Subotnik, J. E.; Thom, A. J. W.; Tkatchenko, A.; Truhlar, D. G.; Van Voorhis, T.; Wesolowski, T. A.; Whaley, K. B.; Woodcock, H. L.; Zimmerman, P. M.; Faraji, S.; Gill, P. M. W.; Head-Gordon, M.; Herbert, J. M.; Krylov, A. I. Software for the Frontiers of Quantum Chemistry: An Overview of Developments in the Q-Chem 5 Package. *J. Chem. Phys.* **2021**, *155* (8), No. 084801.

(33) Hui, K.; Chai, J.-D. SCAN-Based Hybrid and Double-Hybrid Density Functionals from Models without Fitted Parameters. *J. Chem. Phys.* **2016**, *144* (4), No. 044114.

(34) Dunning, T. H. Gaussian Basis Sets for Use in Correlated Molecular Calculations. I. The Atoms Boron through Neon and Hydrogen. *J. Chem. Phys.* **1989**, *90* (2), 1007−1023.

(35) Kendall, R. A.; Dunning, T. H.; Harrison, R. J. Electron Affinities of the First-Row Atoms Revisited. Systematic Basis Sets and Wave Functions. *J. Chem. Phys.* **1992**, *96* (9), 6796−6806.

(36) Wilson, A. K.; Woon, D. E.; Peterson, K. A.; Dunning, T. H. Gaussian Basis Sets for Use in Correlated Molecular Calculations. IX. The Atoms Gallium through Krypton. *J. Chem. Phys.* **1999**, *110* (16), 7667−7676.

(37) Dyall, K. G. Interfacing Relativistic and Nonrelativistic Methods. I. Normalized Elimination of the Small Component in the Modified Dirac Equation. *J. Chem. Phys.* **1997**, *106* (23), 9618−9626.

(38) Kutzelnigg, W.; Liu, W. Quasirelativistic Theory Equivalent to Fully Relativistic Theory. *J. Chem. Phys.* **2005**, *123* (24), No. 241102.

(39) Saue, T. Relativistic Hamiltonians for Chemistry: A Primer. *ChemPhysChem* **2011**, *12* (17), 3077−3094.

(40) Cunha, L. A.; Hait, D.; Kang, R.; Mao, Y.; Head-Gordon, M. Relativistic Orbital-Optimized Density Functional Theory for Accurate Core-Level Spectroscopy. *J. Phys. Chem. Lett.* **2022**, *13* (15), 3438−3449.

(41) Kohn, W.; Sham, L. J. Self-Consistent Equations Including Exchange and Correlation Effects. *Phys. Rev.* **1965**, *140* (4A), No. A1133.

(42) Thomassen, H.; Hedberg, K. Distances, Root-Mean-Square Amplitudes of Vibration, and Vibrational Anharmonicity in Carbon Tetrabromide from a Gas-Phase Electron-Diffraction Investigation. *J. Mol. Struct.* **1990**, *240*, 151−157.

(43) Shimanouchi, T. *Tables of Molecular Vibrational Frequencies Part 1*, National Standard Reference Data Series; National Bureau of Standards, 1967.

(44) Hait, D.; Head-Gordon, M. Orbital Optimized Density Functional Theory for Electronic Excited States. *J. Phys. Chem. Lett.* **2021**, *12* (19), 4517−4529.

(45) Hait, D.; Head-Gordon, M. Excited State Orbital Optimization via Minimizing the Square of the Gradient: General Approach and Application to Singly and Doubly Excited States via Density Functional Theory. *J. Chem. Theory Comput.* **2020**, *16* (3), 1699−1710.

(46) Boo, B. H.; Saito, N.; Suzuki, I. H.; Koyano, I. Dissociation Processes of Core-Excited CBr_4 Involving the Br(3d, 3p, 3s) and C(1s) Inner-Shells in the Range 50−460 eV. *J. Electron Spectrosc. Relat. Phenom.* **2002**, *123* (1), 73−84.

(47) Xu, Z.; Hu, P.; Wang, E.; Xu, S.; Wang, X.; Zhao, Y.; Deng, J.; Ning, C.; Ren, X. Experimental and Theoretical Study of Valence Electronic Structure of Tetrabromomethane by (e, 2 e) Electron Momentum Spectroscopy. *Phys. Rev. A* **2019**, *99* (6), No. 062705.